Journal Pre-proof

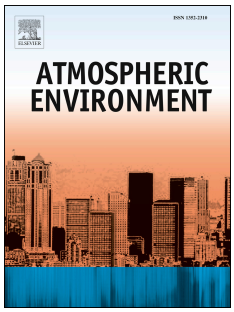

Parametric analysis for global single scattering albedo calculations

Jaein I. Jeong, Duseong S. Jo, Rokjin J. Park, Hyung-Min Lee, Gabriele Curci, Sang-Woo Kim

PII: S1352-2310(20)30350-2

DOI: https://doi.org/10.1016/j.atmosenv.2020.117616

Reference: AEA 117616

To appear in: *Atmospheric Environment*

Received Date: 15 November 2019

Revised Date: 12 May 2020

Accepted Date: 15 May 2020

Please cite this article as: Jeong, J.I., Jo, D.S., Park, R.J., Lee, H.-M., Curci, G., Kim, S.-W., Parametric analysis for global single scattering albedo calculations, *Atmospheric Environment* (2020), doi: https://doi.org/10.1016/j.atmosenv.2020.117616.

CRediT authorship contribution statement

Jaein I. Jeong: Writing - original draft, Visualization, Writing - review & editing. **Duseong S. Jo:** Writing - original draft, Conceptualization, Software, Visualization, Writing - review & editing. **Rokjin J. Park:** Supervision, Conceptualization, Methodology, Writing - review & editing. **Hyung-Min Lee:** Investigation, Writing - review & editing. **Gabriele Curci:** Software, Writing - review & editing. **Sang-Woo Kim:** Investigation, Writing - review & editing.

Parametric analysis for global single scattering albedo calculations

Jaein I. Jeong[1], Duseong S. Jo[2,3], Rokjin J. Park[1*], Hyung-Min Lee[1], Gabriele Curci[4,5], and Sang-Woo Kim[1]

[1]School of Earth and Environmental Sciences, Seoul National University, Seoul, South Korea

[2]Cooperative Institute for Research in Environmental Sciences, University of Colorado, Boulder, CO, USA

[3]Department of Chemistry, University of Colorado, Boulder, CO, USA

[4]Department of Physical and Chemical Sciences, University of L'Aquila, L'Aquila, Italy

[5]Center of Excellence in Telesensing of Environment and Model Prediction of Severe Events, University of L'Aquila, L'Aquila, Italy

A paper submitted to Atmospheric Environment

*Corresponding author address: Rokjin J. Park, School of Earth and Environmental Sciences, Seoul National University, 1 Gwanak-ro, Gwanak-gu, Seoul 08826, South Korea.

Email: rjpark@snu.ac.kr

Abstract

Single scatter albedo (SSA) is a key parameter in radiative transport models for estimating aerosol direct radiative forcing (DRF) and is also a major contributor to DRF uncertainty. We investigate the sensitivity of SSA calculations to physical input parameters (e.g., mixing state, size distribution, density, and refractive index of aerosols) associated with absorbing aerosols (e.g., black carbon [BC], brown carbon [BrC], and soil dust). We attempted to estimate global aerosol SSAs using the 3-D global chemical transport model (GEOS-Chem) and a post-processing tool of aerosol optical properties (FlexAOD) and evaluated the model by comparing it with observed values. The model reproduces the observed variability of both the surface aerosol concentrations and aerosol optical depth (AOD) obtained from the Surface Particulate Matter Network (SPARTAN), the global Aerosol Mass Spectrometer (AMS), and the Aerosol Robotic Network (AERONET). Our sensitivity tests show that the physical input parameters, which are not as well understood as aerosol mass concentrations, can lead to large uncertainties in global SSA values. We find that BC mixing state, BrC, and a dust size distribution have significant impacts on the global SSA calculation. Their combined use can reduce aerosol SSA bias in the model by 43% at 440 nm, compared to observations. We also find that the direct radiative effect (DRE) of global aerosols increases by 10% (from -2.62 W m^{-2} to -2.36 W m^{-2}) when the SSA bias is corrected.

Keywords: Black carbon; Brown carbon; Single scattering albedo; Direct radiative effect

1. Introduction

Aerosol optical depth (AOD), asymmetry parameter, and single scattering albedo (SSA) are key input variables required to calculate the aerosol direct radiative forcing (DRF) (Jacobson, 2001). In particular, SSA is an essential parameter for estimating DRF because even small changes in SSA cause a significant change in DRF, and SSA may also determine the sign of DRF. For example, if SSA changes from 0.8 to 0.9, DRF may change from positive (warming effect) to negative (cooling effect) (Hansen et al., 1997).

In general, the calculation of SSA relies on the Mie theory, which is widely used in atmospheric chemistry models due to its simplicity, computational efficiency, and ease of application in the radiative transfer model. The Mie theory for SSA calculations requires input parameters such as aerosol size distributions, density, hygroscopic growth factors, and refractive index. However, since aerosol characteristics vary greatly depending on mixing state, aging, source, and region, SSA estimation using models has high uncertainties. Although the development of measurement techniques and the use of aerosol observations can reduce such uncertainties, it is still challenging to determine the best combination of physical parameters for aerosol simulation models. Also, physical assumptions significantly affect SSA calculations. For example, a global modeling study reported similar SSA values between model and aerosol robot network (AERONET) observation (Chin et al., 2009), whereas others suggest a positive bias in the model SSA (Jo et al., 2016; Myhre et al., 2009). The difference in their findings is mainly due to different black carbon (BC) densities and emissions, i.e., the low SSA bias presented by Chin et al. (2009) is due to the relatively low BC density and high BC emissions. Their BC density of 1.0 g cm^{-3} is the lowest in the literature, and the global BC emission of 10.2 Tg C yr^{-1} was also 50% higher than that of Jo et al. (2016). The differences in aerosol emissions and physical parameters, as in the example above, make it challenging to identify the significant factors that affect SSA calculation.

SSA depends on the mixing state, particle shape, wavelength, and mass ratio of non-black carbon to black carbon (Liu et al., 2017). Therefore, selecting the best parameters for BC in the Mie calculation is a more important issue than other aerosols, because BC is an aggregate composed of several small spherical particles. However, the AeroCom model intercomparison project reveals significant differences in BC

information: refractive index (1.75-0.44i − 2.0-1.0i), density (1.0 − 2.0 g cm^{-3}), and particle size (0.020 − 0.852 μm) (Koch et al., 2009).

Although BC predominantly contributes to aerosol absorption, soil dust is also a significant contributor because the total global burden of soil dust is much higher than other aerosols (Yang et al., 2009). Despite its importance, the effects of dust size distribution on SSA in global models were poorly evaluated (Kok et al., 2017). Also, recent studies have focused on the absorption of brown carbon (BrC) (Jo et al., 2016; Park et al., 2010). BrC plays an essential role in SSA calculations, but few models take into account the absorption of BrC.

In this study, we focus on four major factors (e.g., aerosols mixing state for the Mie scattering calculations, size distribution and refractive index of BC, size distribution of soil dust, and BrC) that may influence SSA estimation. First, we extensively evaluate the aerosol mass concentrations in surface air and optical values using global aerosol observation network data, namely the Surface Particulate Matter Network (SPARTAN) (Snider et al., 2015), the global Aerosol Mass Spectrometer (AMS) (Zhang et al., 2007), and AERONET, as seen in Figs. S1, S2, and S3, respectively. We perform sensitivity simulations to investigate their effects on SSA. Finally, we use the best model result to estimate the global aerosol direct radiative effect (DRE) and provide implications for the climate effects of current general circulation models (GCMs).

2. Global model and data

2.1. GEOS-Chem

We used a 3-D global chemical transport model (GEOS-Chem; version 10-01-01) with the Modern Era Retrospective-analysis for Research and Applications (MERRA) reanalysis meteorological fields. MERRA provides meteorological data such as wind, temperature, planetary boundary layer height, humidity, and other variables on a horizontal scale of 0.5° × 0.667°. Although the details of the spatial structure are reduced, we used re-grided data with a horizontal scale of 2° × 2.5° to improve the computational efficiency of the global model simulation.

The anthropogenic emissions of OC, BC, SO_2, NO_X, NH_3, and CO used

hemispherical air pollution (HTAP) v2 inventory, which includes a ship, energy, industrial, transportation, residential, and agricultural sector data (Janssens-Maenhout et al., 2015). HTAP v2 has a horizontal resolution of 0.1° × 0.1°, and the reference year was taken as 2010. We applied a diurnal variation of NH_3 to reduce the overestimation of nitrate aerosol in the model (Zhu et al., 2015). Aromatics of benzene, toluene, and xylenes used the Reanalysis of the Tropospheric chemical composition (RETRO) emission inventory (Schultz et al., 2007). The biogenic VOC emission follows the Model of Emissions of Gases and Aerosols from Nature (MEGAN) v2.1 (Guenther et al., 2012). The biogenic VOC emission is calculated based on the canopy environment, soil moisture, emission factors, and leafage. The biomass burning emission is estimated using the Global Fire Emission Database Version 4 (GFEDv4) inventory with monthly time resolution and a spatial resolution of 0.25° × 0.25° (Giglio et al., 2013). Table 1 summarizes the global anthropogenic and natural emissions used in this study.

We performed fully-coupled Ox-NOx-hydrocarbon-aerosol simulations. The model considers both anthropogenic aerosols such as BC, OC, ammonium, sulfate, and nitrate, and natural aerosols of soil dust and sea salt. The generation of BC and OC is based on the methods described by Park et al. (2003), and the transition from hydrophobic to hydrophilic tracers assumes an e-folding time scale of 1.15 days. Secondary organic aerosol (SOA) follows the scheme proposed by Pye et al. (2010), which regards hydrocarbons of a monoterpene, sesquiterpene, isoprene, and aromatic compounds as NOx-dependent yields. More detailed information on SOA generation is described in Pye et al. (2010).

We calculated the BrC concentration in both the primary and secondary sources using the calculated 3-D global BrC to OC ratio produced by Jo et al. (2016). The mean ratio of vertically integrated BrC to OC was 0.19 on the global scale but can vary locally (Jo et al., 2016). They calculated the global BrC to OC ratios of biofuel and biomass burning emissions from the relationship between the absorption Angstrom exponent and the modified combustion efficiency. We also applied the refractive indices of BrC proposed by Jo et al. (2016) to estimate BrC absorption. A detailed method and global distribution of BrC can be found in Jo et al. (2016).

Secondary inorganic aerosols such as sulfate, nitrate, and ammonium are calculated

using ISORROPIA II, which considers thermodynamic equilibrium for HNO_3-H_2SO_4-NH_3-H_2O (Fountoukis and Nenes, 2007). The model used the dust entrainment and deposition (DEAD) scheme proposed by Zender et al. (2003) for soil dust generation, which follows the source function from the GOCART model (Chin et al., 2002; Fairlie et al., 2007). The sea salt particles are produced as a function of the sea surface temperature with 10 m wind speed (Alexander et al., 2005; Gong, 2003).

Secondary inorganic and carbonaceous aerosols are simulated using a bulk aerosol technique that only computes mass concentrations. Number concentrations are calculated using the constant density of each aerosol. Size distributions assume a log-normal distribution and are calculated using the geometric mean radius and standard deviation of each aerosol (Table 2). On the other hand, sea salt and dust aerosols are divided into two bins and four bins, respectively, depending on the particle size.

2.2. Aerosol data

We evaluate the model by using observations of surface aerosol mass concentrations, aerosol chemical compositions, and aerosol optical properties from the SPARTAN, the AMS dataset, and the AERONET, respectively. The SPARTAN is a global network for observing particulate matter mass concentrations and optical properties designed to validate satellite remote sensing estimates for application to health impact studies and risk assessments and to reduce the current gap in knowledge of global aerosol concentrations. The SPARTAN sites are primarily located in populated areas and are deployed in conjunction with the AERONET, a ground-based optical network that measures AOD. Each site has a filter sampler that measures the concentration of $PM_{2.5}$ and PM_{10}, and a three-wavelength integrating nephelometer that measures the light scattering of the aerosol. The SPARTAN filters also measure water-soluble ions, OC and elemental carbon, and trace elements.

The global AMS dataset provides aerosol concentrations observed from the ground between 2000 and 2008, with multiple sites located primarily in the Northern Hemisphere classified as urban, downwind, and rural regions. Spracklen et al. (2011) compiled ten additional datasets into the AMS observations compiled by Zhang et al. (2007), providing a total of 47 observations at 34 separate locations. Each observation is

sampled continuously from the ground and is usually an average of one month. The AMS measures the specified PM mass concentrations and size distributions through the inlet system that generates the particle beam, the particle sizing section, and the particle composition analysis section. The AMS measurement technique is described in detail in Canagaratna et al. (2007).

The AERONET is a ground-based remote sensing aerosol network established in the 1990s and is a well-developed facility for passive aerosol measurement (Holben et al., 1998). The AERONET consists of the same sunphotometers at hundreds of sites globally and provides time-series data with a very high time resolution over the years. The AERONET measures aerosol extinctions, typically every 15 minutes at eight wavelengths (340, 380, 440, 500, 675, 870, 1020, and 1640 nm) and provides AOD, SSA, precipitable water vapor, aerosol size distribution, and refractive index. It is noted that from 2008 to 2010, only wavelengths of 440, 675, 870, and 1020 nm were retrieved for SSA. Version 3 data are available at three levels: level 1, 1.5, and 2, which present raw data, cloud-screened and quality controlled data, and quality-assured data, respectively. This study uses level 2 data to evaluate the model results.

3. Estimation of aerosol optical properties

3.1. FlexAOD

We calculated the aerosol optical properties, including AOD, SSA, and asymmetric parameters using the Flexible Aerosol Optical Depth (FlexAOD), which is a post-processing tool for aerosol optical property calculations in GEOS-Chem (Curci et al., 2019; Curci et al., 2015). FlexAOD calculates the aerosol optical properties using Mie theory with input data, including refractive indices, size distributions, hygroscopic growth factors, and particle density for each aerosol species. All aerosol species are assumed to be distributed as a lognormal function, except for the dust with gamma distribution used.

FlexAOD can be used to calculate aerosol optical properties in various mixed states. Here, we considered one external and two internal aerosol mixing states for the Mie calculations. In the case of external mixing, each aerosol was assumed to be formed by a single chemical species. In the case of internal mixing, we used two internal mixing

representations: homogeneous and core-shell. The homogeneous internal mixing assumed that all aerosols were well mixed, and the core-shell internal mixing assumed that a concentric well mixed soluble shell coated an insoluble well-mixed core. For the calculation of the optical properties in the internal mixing case, the size distributions were geometrically divided into 100 bins. Then, the mass of each aerosol species was summed in each bin, in order to ensure mass conservation and consistency with external mixing calculation. In each bin, the refractive index was calculated as a volume-weighted average, considering the hygroscopic growth effect of each aerosol species, in each bin. In the case of core-shell, the sum of mass and refractive index average is done separately for the core and the shell. This way, the core mass fraction is allowed to vary as a function of particle size, according to the ratio of core/shell volume in each size bin (Curci et al., 2019, Fig. 4 therein).

For homogeneous internal mixing, Mishchenko et al. (1999) code was used to calculate Mie efficiency (scattering, absorption, and extinction) in each bin. In the case of core-shell internal mixing, the same averaging procedure was applied to the core and the shell separately, and the volume ratio of the core and the shell of the stratified spheres were calculated using the Toon and Ackerman (1981) code. The hydrophobic OC constitutes the core, and the hydrophilic OC assumes a shell to calculate the internal mixing. BC is assumed to be the core regardless of hygroscopicity, and inorganic, dust, and sea salt aerosols are assumed to be the shell. Details of the calculation of aerosol optical properties with different mixing states are described in Curci et al. (2015, 2019).

Table 2 summarizes the input values used in FlexAOD. To improve the SSA calculation in this study, we updated the input values as follows: the geometric standard deviations of sulfate, nitrate, ammonium, BC, and OC were changed from 2.0 to 1.6 based on the values measured by an optical particle counter (Drury et al., 2010). The hygroscopic growth factors (HGFs) and refractive indices of sulfate, nitrate, and ammonium aerosols follow the OPAC database. The HGFs in OC are updated to 1.35 when RH is 95%, based on field and laboratory experiments (Jimenez et al., 2009). The geometric mean radius and density for individual spherules of aggregated BC increased from 0.012 μm to 0.020 μm and from 1.0 g cm^{-3} to 1.8 g cm^{-3}, respectively (Bond and Bergstrom, 2006; Hess et al., 1998). The changes in aerosol absorption from the changes

in BC input values will be discussed in the next section. In this study, wavelength-dependent refractive indices are used, and the values of 440 nm and 870 nm used for model verification are also listed in Table 2.

3.2. Characteristics of BC

Since BC generally has a diverse geometrical size, it is not easy to choose the appropriate BC radius for Mie calculations (Koch et al., 2009). Here, we assumed that individual primary spherules of aggregated BC have a spherical shape. We then investigated the effects of the geometric mean radius (r_g) and geometric standard deviation (σ) on the sensitivity of the BC absorption to select the appropriate BC radius for SSA calculation. We calculated the sensitivity of absorbing AOD (AAOD) for r_g of 1–200 nm, for σ of 1.2, 1.6, 2.0, and for BC burden of 0.25 mg m^{-2} (Fig. 1a). The blue rectangle and red star symbols represent the AAOD values calculated by the size distributions of BC for GEOS-Chem and OPAC, respectively. However, these two size distributions have a very similar AAOD (<1% difference) due to the combined effect of a decrease in r_g and an increase in σ.

Fig. 1b shows the BC AAOD calculated as a function of the refractive indices of real and imaginary parts. The BC AAOD increased with the decrease of the real part and an increase of the imaginary part. The blue triangle and red star represent the BC AAOD values using the refractive index of Bond and Bergstrom (2006) (1.95 – 0.79i) and OPAC (1.74 – 0.44i), respectively. BC AAOD using the refractive index of OPAC was 33% lower than that of Bond and Bergstrom (2006). Similar to our results, the BC AAOD with a refractive index of 1.74 – 0.44i was 29% lower than that of 1.95 – 0.79i in the ECHAM5-HAM model (Stier et al., 2007).

3.3. FlexAOD simulation

The sensitivity experiments of FlexAOD for changing input parameters are performed using aerosol mass concentrations from GEOS-Chem. Here we focused on BC aerosol, which is known to have high absorption. Table 3 shows the lists of the sensitivity experiment for changing input parameters related to BC. For example, GEOS represents the FlexAOD simulation with input parameter values used in GEOS-Chem

v10-01-01. OPAC uses the values from the OPAC database. BB, BBR, and BBHR cases use the same refractive index of 1.95 – 0.79i, but the geometric radius of BC is different. The size of 0.065 μm (BBR) was based on Bond et al. (2013), and an additional geometric mean radius of 0.1 μm (BBHR) was also investigated (Koch et al., 2009).

We also considered the different mixing states, brown carbon, and dust size distributions and added tag names to distinguish them. As previously mentioned, we included three aerosol mixing states: external, homogeneous internal, and core-shell internal with the tags "_EX", "_HI", "_CS", respectively. We added the "_BR" tag if it contains BrC absorption. We also conducted a sensitivity test by changing soil dust size distributions presented from a previous study (Zhang et al., 2013). However, the sensitivity simulation of the dust size distribution applies only to the calculation of the dust optical properties. Dry and wet depositions may alter the mass concentration in the sub-micron size, but the effects on total dust mass concentrations are negligible (Ridley et al., 2012). The "_DI" tag applies to the change in dust size distributions proposed by Zhang et al. (2013). For example, "GEOS_BR_DI_HI" means that input parameters from GEOS-Chem, BrC, soil dust size distributions from Zhang et al. (2013), and homogeneous internal mixing assumptions are used. Detailed descriptions of the sensitivity experiment are summarized in Table A1.

4. Global model evaluation

4.1. Aerosol mass concentrations

We evaluated global aerosol concentrations using AMS and SPARTAN. Since the observations were conducted over different periods (AMS: 2000–2008, SPARTAN: 2013–2015), we focused only on the period of 2008-2010. Therefore, our model is evaluated only with the observed monthly mean values and without considering the year-to-year variability.

Fig. 2 compares the monthly mean concentrations of simulated sulfate, nitrate, ammonium, and OC aerosols with AMS surface observations. The statistical values related to the model evaluations are also shown in Table 4. We found that the model well reproduces the observed sulfate, nitrate, and ammonium concentrations with regression

slopes of 0.69–0.84 and correlation coefficients of 0.62–0.78. However, the simulated OC concentration shows a relatively high RMSE (4.77 μg m^{-3}) and low correlation coefficient (0.36). This result is consistent with AMS observations reported in previous studies (Jo et al., 2013; Yu, 2011). They suggested that the negative bias of OC is mainly due to poor SOA simulations, which was also presented in the AeroCom intercomparison project (Tsigaridis et al., 2014).

Fig. 3 and Table 4 show a comparison between the model and SPARTAN observations. The results are worse than those with AMS observations, especially for nitrate aerosol, because the observations were collected in different periods. Since both NO_x emissions and nitrate concentrations in the United States and Europe show decreasing trends, observations from these two different periods are likely to have different levels of nitrate concentration. Nitrate overestimation appears mainly in the United States (7 points above the 10:1 line) and South East Asia (7 points above the 10:1 line) and is consistent with previous studies in East Asia (Wang et al., 2013), South Asia (Gu et al., 2016), and the United States (Schiferl et al., 2014; Zhu et al., 2013) using GEOS-Chem model. Although there are efforts to reduce the nitrate overestimation in the model (e.g., boundary layer height, dry deposition velocity, and the reaction rate of nitric acid), this issue is still not fully-resolved (Zhu et al., 2013). Recent AeroCom phase III study also suggests that nitrate has enormous diversity in inorganic aerosol simulations (Bian et al., 2017). However, finding a solution to the overestimation of nitrate is beyond the scope of this study.

Simulated BC shows a regression slope of 0.94, which is a relatively better result compared to nitrate. However, the BC concentration is underestimated by 37%, mainly in Manila (10 points below the 1:10 line). The errors can be attributed to a poor geographical representation of the model because this site is mostly assigned to the high ratio (>75%) of the ocean in the model grid box (Fig. S4). The model spatial resolution (2° × 2.5°) is too coarse to capture the local sources, especially the island. This discrepancy is improved by using the finer spatial resolution (e.g., 0.25° × 0.3125°) of the GEOS-Chem model (Chen et al., 2009; Yu et al., 2016).

We estimated the observed soil dust concentration according to the SPARTAN speciation proposed by Snider et al. (2016). They estimated the soil dust mass by

multiplying the [Mg + Fe + Al] concentration by 10, based on the element composition of soil dust proposed by Wang (2015). Although it is straightforward, we find that the soil dust concentration derived from this method is similar to Malm et al. (1994) based on the observed dust concentration (regression slope 1.0, R = 0.98). The simulated $PM_{2.5}$ concentrations are similar to the observations but with slightly lower bias (24% lower mean concentration, R = 0.76). The model well reproduces the observed aerosol concentrations, but slightly underestimates or overestimates depending on species and sites. Therefore, we excluded some observations with high errors by some criteria described in the next section.

4.2. SSA and AOD

As described above, the model well captured the observed $PM_{2.5}$ concentrations (R=0.76). However, the results can be affected by the overestimation of nitrate and the underestimation of OC. Therefore, to increase the reliability of the model for SSA and AOD, we removed the AERONET sites that do not meet the following criteria: (1) The difference between the monthly mean aerosol concentration of the model and the observations should be less than a factor of two at surface networks (AMS and SPARTAN); and (2) AMS (or SPARTAN) and AERONET sites must be on the same or adjacent model grid. This will improve the reliability of the results derived from the model by using more similar model values for observation, although the number of data used is reduced.

Fig. 4a shows the observed and simulated AOD at 500 nm for the baseline case (GEOS_EX). The AOD statistics between the observation and the model is similar to the result of $PM_{2.5}$. The correlation coefficients for AOD and $PM_{2.5}$ are both 0.76; the slopes are 0.68 and 0.70; and the normalized mean bias (NMB) values are -20% and -24%, respectively. From these results, we concluded that there are no significant errors in simulated aerosol concentration (GEOS-Chem) and aerosol optical characterization (FlexAOD). When using the filtering data satisfying the above criteria, the model shows improved statistics for the observed values at the AERONET sites with the correlation coefficient increasing to 0.82, and NMB decreasing to -10% (Fig. 4b).

Figs. 5a and 5b show the SSA comparison between the observation and the model at all AERONET sites at 440 nm and 870 nm wavelengths, respectively. In this study, we excluded SSAs value when AOD is less than 0.4 because the uncertainty of SSA retrieval is high for low AODs (Dubovik et al., 2002). The model well simulates the observed SSA at 870 nm but slightly overestimates the observed SSA at 440 nm. The mean SSA of the model (0.95) is 0.05 higher than the observation (0.90) at 440 nm. The model underestimates BC and scattering aerosols ($PM_{2.5}$ minus BC) by 37% and 23%, respectively. The underestimation of BC (scattering aerosols) overestimates (underestimates) the SSA, which can offset the simulated SSA error. Therefore, it can be inferred that the overestimation of SSA was caused by other factors. This SSA overestimation is also discussed by Jo et al. (2016), and they found that the SSA produced by GEOS-Chem overestimated the AERONET observations. The next section examines the reason for this overestimation of SSA.

Figs. 5c and 5d are similar to Figs. 5a and 5b, but only using AERONET data that meet the two criteria described above. The model shows an improved SSA at 440 nm with increasing correlation coefficient from 0.34 to 0.50. The improved results are also seen in the evaluation of AOD at 500 nm (Fig. 4b), but the model does not show improved SSA at 870 nm. Although some wavelengths did not show improvement in SSA, the results for AOD at 500 nm and SSA at 440 nm are improved using selected AERONET sites. Therefore, we use only filtered AERONET data for sensitivity studies below.

5. Influence of parameters in global SSA simulation

In this section, we discuss the sensitivity analysis of aerosol characteristics including mixing state, BrC, and soil dust size distributions on SSA values. We also examine the sensitivity to the physical properties of BC, but there are no significant differences (Fig. S5). We compare the model SSA values at 440 and 870 nm with the AERONET observations.

Fig. 6 shows the effect of BC internal mixing on global SSA calculation. We found that both homogeneous internal mixing (GEOS_HI; Fig. 6a) and core-shell

internal mixing (GEOS_CS; Fig. 6b) significantly reduce SSA (GEOS_HI: 0.85 and GEOS_CS: 0.84) at 440 nm (see Table 5). Also, the NMBs of the AODs of internal mixing (GEOS_HI: -0.13 and GEOS_CS: -0.13) are larger than those of external mixing (GEOS_EX: -0.03) at 500 nm (see Table S1). AOD also significantly decreases when using internal mixing rather than external mixing. The main reason for these results is a decrease in the aerosol number concentration with increasing aerosol size, which is similar to the previous result published by Curci et al. (2015).

Considerations for BrC absorption (GEOS_BR_EX) and change in soil dust size distribution (GEOS_DI_EX) both reduce the overestimation of SSA (Figs. 6c-d). Compared to SSA in the baseline simulation (GEOS_EX) at 440 nm, the global mean SSAs for GEOS_BR_EX and GEOS_DI_EX decrease by 0.015 and 0.008, respectively, and the regression slopes increase from 0.38 to 0.55 and 0.67, respectively. The correlation of GEOS_BR_EX slightly increases (R = 0.56), whereas GEOS_DI_EX decreases (R = 0.34). Unlike the SSA results, there is no significant AOD reduction (-7% – 1%) compared to GEOS_EX (see Table S1).

Fig. 7 shows the SSA sensitivity at 440 nm, considering both BrC absorption and soil dust size distribution. Although SSA overestimation remains in the model, all four sensitivity cases show improved SSA compared to the baseline simulation. Based on these results, we suggest that the SSA gap between the model and the observation be reduced by assuming strong BrC absorption (Chung et al., 2012). However, since BrC absorption varies widely in the region (Jo et al., 2016), it is still unclear whether BrC is globally dominant. Therefore, further studies are needed to improve the accuracy of BrC concentration to better understand the effect of BrC on SSA.

We also found that increasing the geometric mean radius of BC reduces correlation coefficient and regression slope. This result implies that using a small spherical radius (~ 0.02 μm) of BC in the Mie theory is more appropriate than a large radius (~ 0.1 μm). Although the spherical Mie theory is not appropriate for calculating BC optical properties because BC generally forms aggregates rather than spheres, the use of a BC radius of 0.02 μm in the global model can provide better SSA results. However, SSA at 870 nm shows quite different results from 440 nm because BC has a more dominant influence on aerosol absorption than dust or BrC at 870 nm. Yang et al. (2009)

reported that the mass absorption efficiency of BC (5.9 $m^2 g^{-1}$) at 880 nm was higher than that of dust (0.001 $m^2 g^{-1}$) or BrC (0.02 $m^2 g^{-1}$). The difference is mainly due to the refractive index and size distribution of BC. We found out that the effects of the refractive index of BC on SSA are more pronounced at 870 nm than at 440 nm. For example, when we use a higher refractive index (BB_BR_DI_EX), the SSA at 870 nm is reduced by 0.02, and the absolute magnitude of the decrease is more significant than at 440 nm (-0.01) (Table 6). Based on several sensitivity results for AOD and SSA, we found that the GEOS_BR_DI_EX case shows the best model performance for AERONET observations. The DRE calculated using GEOS_BR_DI_EX will be discussed in the next section.

6. Implications for Global DRE

In this section, we calculated the clear-sky global DRE using the input parameters selected in the previous section. Fig. 9a shows the annual mean global DRE from the baseline simulation (GEOS_EX) for 2008-2010. The result shows negative values globally, except for North Africa, where there is weak absorption due to high dust aerosols. The absolute values of high DRE are found in areas with high levels of anthropogenic (East Asia) and biomass burning (Central Africa) emissions. The global mean DRE (-2.62 W m^{-2}) is equal to the previous work (-2.62 W m^{-2}) by Heald et al. (2014).

The absorption by BrC (GEOS_BR_EX) increases the annual mean global DRE by 0.07 W m^{-2}, especially in regions with high biofuel (East Asia) and biomass burning (Central Africa) emissions. However, we assumed that the increase in global DRE by BrC may be higher than 0.07 W m^{-2}, because the simulated BrC absorption may be underestimated (see section 5). The annual mean global DRE increases by 0.17 W m^{-2} (Fig. 9f) due to changes in the soil dust size distribution (GEOS_DI_EX), which is more than twice the DRE increase due to BrC absorption. Finally, considering both the absorption of BrC and the change in soil dust size distribution (GEOS_BR_DI_EX), the DRE increases by 0.26 W m^{-2} (Fig. 9g), which accounts for 10% of the annual mean global DRE of the baseline case (GEOS_EX).

SSA changes compared to GEOS_EX at 440 nm showed that the effects of BrC absorption (-0.02) are relatively higher than that of the dust size distribution change (-

0.01) (see Table 5). However, the relatively high DRE change (0.17) is mainly due to the soil dust burden (14.4 Tg), which is 10–100 times higher than OC (1.4 Tg) and BC (0.1 Tg) (Fig. 9f). Therefore, unlike SSA, we found out that soil dust size distribution plays an important role in estimating the global DRE of the model, which is similar to Kok et al. (2017).

7. Summary and discussion

In this study, we examined the effects of four input variables, namely mixing state, physical parameters of BC, soil dust size distribution, and BrC, to the global SSA estimation using the GEOS-Chem and FlexAOD. First, we evaluated the model extensively using surface aerosol concentrations (AMS and SPARTAN networks) and AOD (AERONET). We then examined the effect of input parameters on the global SSA using sensitivity experiments and observations at 440 nm and 870 nm. We found that the combination of external mixing state, BrC, and observational basis of soil size distribution provides the best performance model, compared to AERONET SSA and AOD. However, it is difficult to determine whether the input parameters derived from these results can be directly applied to other global models. Although not discussed in detail in this study, other factors affect global SSA and AOD calculations, such as hygroscopic growth factors. We propose some notable results that can be applied to the use of the Mie theory for calculating aerosol optical properties in the chemical transport models:

1. The influence of input parameters of OPAC and Bond and Bergstrom (2006) did not show any significant difference in BC absorption. However, the refractive index used in the former (1.74 – 0.44i) is lower than the latter (1.95 – 0.79i), and the BC absorption of OPAC is 33% lower than that of Bond and Bergstrom (2006). The relatively low BC particle density (1.0 g cm^{-3}) used by OPAC causes relatively high number concentration, which may lead to increased AOD and absorption of BC. We found that the global mean SSA using OPAC, 0.93, is similar to that of Bond and Bergstrom (2006), 0.93. Although previous studies related to global optical properties did not provide the density of BC used in their Mie calculations, BC density is an important factor in SSA estimation and is one of the variables that must be emphasized in future

model intercomparison studies.

2. The assumption of the external mixing state shows better global optical results than that of the internal mixing state. The internal mixing state causes high absorption and results in an underestimation of the model SSA compared to AERONET observations. SSA underestimation by the internal mixing state has also been reported in previous studies such as aircraft observations and laboratory measurements (Cappa et al., 2012; Drury et al., 2010). However, the effects of BC absorption due to the internal mixing state can also vary depending on the region, coating thickness, aging time, and distance from the source (Liu et al., 2015). Therefore, future modeling studies need to consider region-specific mixing states to derive optimal optical results.

3. The characteristics of SSA differ at different wavelengths. However, in previous modeling studies, SSAs were mostly compared with observations at wavelengths of 440-550 nm (Dai et al., 2015; Lin et al., 2014). Therefore, we suggest that shorter or longer wavelengths should be considered while evaluating the overall effects of aerosols on SSA.

4. Global models should take into account both the BrC absorption and observation-based dust size distribution. These factors reduce the SSA at short wavelengths, thereby reducing the positive SSA bias at 440 nm found in previous global modeling studies (Jo et al., 2016; Lin et al., 2014).

5. The global annual mean DRE is significantly increased (0.17 W m^{-2}) by observation-based dust size distribution, which is more than twice as high as the DRE increase due to BrC absorption (0.07 W m^{-2}). We propose that an improved soil dust size distribution based on observations be applied to global DRF estimates.

Acknowledgment

We thank anonymous reviewers for their helpful comments on the manuscript. We thank the principal investigators and their staff for establishing and maintaining the SPARTAN, AMS, and AERONET sites used in this study. This work was supported by the National Strategic Project-Fine particle of the National Research Foundation of Korea (NRF) funded by the Ministry of Science and ICT (MSIT), the Ministry of Environment (ME),

521 and the Ministry of Health and Welfare (MOHW) (NRF-2017M3D8A1090670).

522

523

524 **References**

525

526 Alexander, B., Park, R.J., Jacob, D.J., Li, Q.B., Yantosca, R.M., Savarino, J., Lee, C.C.W., Thiemens,
527 M.H., 2005. Sulfate formation in sea-salt aerosols: Constraints from oxygen isotopes. Journal of
528 Geophysical Research D: Atmospheres 110, 1-12, doi:10.1029/2004JD005659.

529 Bian, H., Chin, M., Hauglustaine, D.A., Schulz, M., Myhre, G., Bauer, S.E., Lund, M.T., Karydis,
530 V.A., Kucsera, T.L., Pan, X., Pozzer, A., Skeie, R.B., Steenrod, S.D., Sudo, K., Tsigaridis, K.,
531 Tsimpidi, A.P., Tsyro, S.G., 2017. Investigation of global particulate nitrate from the AeroCom
532 phase III experiment. Atmospheric Chemistry and Physics 17, 12911-12940, doi:10.5194/acp-
533 17-12911-2017.

534 Bond, T.C., Bergstrom, R.W., 2006. Light absorption by carbonaceous particles: An investigative
535 review. Aerosol Science and Technology 40, 27-67, doi:10.1080/02786820500421521.

536 Bond, T.C., Doherty, S.J., Fahey, D.W., Forster, P.M., Berntsen, T., Deangelo, B.J., Flanner, M.G.,
537 Ghan, S., Kärcher, B., Koch, D., Kinne, S., Kondo, Y., Quinn, P.K., Sarofim, M.C., Schultz, M.G.,
538 Schulz, M., Venkataraman, C., Zhang, H., Zhang, S., Bellouin, N., Guttikunda, S.K., Hopke, P.K.,
539 Jacobson, M.Z., Kaiser, J.W., Klimont, Z., Lohmann, U., Schwarz, J.P., Shindell, D., Storelvmo, T.,
540 Warren, S.G., Zender, C.S., 2013. Bounding the role of black carbon in the climate system: A
541 scientific assessment. Journal of Geophysical Research Atmospheres 118, 5380-5552,
542 doi:10.1002/jgrd.50171.

543 Canagaratna, M.R., Jayne, J.T., Jimenez, J.L., Allan, J.D., Alfarra, M.R., Zhang, Q., Onasch, T.B.,
544 Drewnick, F., Coe, H., Middlebrook, A., Delia, A., Williams, L.R., Trimborn, A.M., Northway,
545 M.J., DeCarlo, P.F., Kolb, C.E., Davidovits, P., Worsnop, D.R., 2007. Chemical and microphysical
546 characterization of ambient aerosols with the aerodyne aerosol mass spectrometer. Mass
547 Spectrom Rev 26, 185-222, doi:10.1002/mas.20115.

548 Cappa, C.D., Onasch, T.B., Massoli, P., Worsnop, D.R., Bates, T.S., Cross, E.S., Davidovits, P.,
549 Hakala, J., Hayden, K.L., Jobson, B.T., Kolesar, K.R., Lack, D.A., Lerner, B.M., Li, S.M., Mellon,
550 D., Nuaaman, I., Olfert, J.S., Petäjä, T., Quinn, P.K., Song, C., Subramanian, R., Williams, E.J.,
551 Zaveri, R.A., 2012. Radiative absorption enhancements due to the mixing state of atmospheric
552 black carbon. Science 337, 1078-1081, doi:10.1126/science.1223447.

553 Chen, D., Wang, Y., McElroy, M.B., He, K., Yantosca, R.M., Le Sager, P., 2009. Regional CO

554 pollution and export in China simulated by the high-resolution nested-grid GEOS-Chem model.
555 Atmospheric Chemistry and Physics 9, 3825-3839, doi:10.5194/acp-9-3825-2009.

556 Chin, M., Diehl, T., Dubovik, O., Eck, T.F., Holben, B.N., Sinyuk, A., Streets, D.G., 2009. Light
557 absorption by pollution, dust, and biomass burning aerosols: A global model study and
558 evaluation with AERONET measurements. Annales Geophysicae 27, 3439-3464,
559 doi:10.5194/angeo-27-3439-2009.

560 Chin, M., Ginoux, P., Kinne, S., Torres, O., Holben, B.N., Duncan, B.N., Martin, R.V., Logan, J.A.,
561 Higurashi, A., Nakajima, T., 2002. Tropospheric aerosol optical thickness from the GOCART
562 model and comparisons with satellite and sun photometer measurements. Journal of the
563 Atmospheric Sciences 59, 461-483.

564 Chung, C.E., Kim, S.W., Lee, M., Yoon, S.C., Lee, S., 2012. Carbonaceous aerosol AAE inferred
565 from in-situ aerosol measurements at the Gosan ABC super site, and the implications for brown
566 carbon aerosol. Atmospheric Chemistry and Physics 12, 6173-6184, doi:10.5194/acp-12-6173-
567 2012.

568 Curci, G., Alyuz, U., Barò, R., Bianconi, R., Bieser, J., H. Christensen, J., Colette, A., Farrow, A.,
569 Francis, X., Jiménez-Guerrero, P., Im, U., Liu, P., Manders, A., Palacios-Peña, L., Prank, M.,
570 Pozzoli, L., Sokhi, R., Solazzo, E., Tuccella, P., Unal, A., Vivanco, M.G., Hogrefe, C., Galmarini,
571 S., 2019. Modelling black carbon absorption of solar radiation: Combining external and internal
572 mixing assumptions. Atmospheric Chemistry and Physics 19, 181-204, doi:10.5194/acp-19-181-
573 2019.

574 Curci, G., Hogrefe, C., Bianconi, R., Im, U., Balzarini, A., Baró, R., Brunner, D., Forkel, R.,
575 Giordano, L., Hirtl, M., Honzak, L., Jiménez-Guerrero, P., Knote, C., Langer, M., Makar, P.A.,
576 Pirovano, G., Pérez, J.L., San José, R., Syrakov, D., Tuccella, P., Werhahn, J., Wolke, R., Žabkar, R.,
577 Zhang, J., Galmarini, S., 2015. Uncertainties of simulated aerosol optical properties induced by
578 assumptions on aerosol physical and chemical properties: An AQMEII-2 perspective.
579 Atmospheric Environment 115, 541-552, doi:10.1016/j.atmosenv.2014.09.009.

580 Dai, T., Shi, G., Nakajima, T., 2015. Analysis and evaluation of the global aerosol optical
581 properties simulated by an online aerosol-coupled non-hydrostatic icosahedral atmospheric
582 model. Advances in Atmospheric Sciences 32, 743-758, doi:10.1007/s00376-014-4098-z.

583 Drury, E., Jacob, D.J., Spurr, R.J.D., Wang, J., Shinozuka, Y., Anderson, B.E., Clarke, A.D., Dibb,

J., McNaughton, C., Weber, R., 2010. Synthesis of satellite (MODIS), aircraft (ICARTT), and surface (IMPROVE, EPA-AQS, AERONET) aerosol observations over eastern North America to improve MODIS aerosol retrievals and constrain surface aerosol concentrations and sources. Journal of Geophysical Research Atmospheres 115, doi:10.1029/2009JD012629.

Dubovik, O., Holben, B., Eck, T.F., Smirnov, A., Kaufman, Y.J., King, M.D., Tanré, D., Slutsker, I., 2002. Variability of absorption and optical properties of key aerosol types observed in worldwide locations. Journal of the Atmospheric Sciences 59, 590-608.

Fairlie, T.D., Jacob, D.J., Park, R.J., 2007. The impact of transpacific transport of mineral dust in the United States. Atmospheric Environment 41, 1251-1266, doi:10.1016/j.atmosenv.2006.09.048.

Fountoukis, C., Nenes, A., 2007. ISORROPIAII: A computationally efficient thermodynamic equilibrium model for K+-Ca2+-Mg2+-NH4 +-Na+-SO4 2--NO3 --Cl--H2O aerosols. Atmospheric Chemistry and Physics 7, 4639-4659.

Giglio, L., Randerson, J.T., Van Der Werf, G.R., 2013. Analysis of daily, monthly, and annual burned area using the fourth-generation global fire emissions database (GFED4). Journal of Geophysical Research: Biogeosciences 118, 317-328, doi:10.1002/jgrg.20042.

Gong, S.L., 2003. A parameterization of sea-salt aerosol source function for sub- and super-micron particles. Global Biogeochemical Cycles 17, 8-1.

Gu, Y., Liao, H., Bian, J., 2016. Summertime nitrate aerosol in the upper troposphere and lower stratosphere over the Tibetan Plateau and the South Asian summer monsoon region. Atmospheric Chemistry and Physics 16, 6641-6663, doi:10.5194/acp-16-6641-2016.

Guenther, A.B., Jiang, X., Heald, C.L., Sakulyanontvittaya, T., Duhl, T., Emmons, L.K., Wang, X., 2012. The model of emissions of gases and aerosols from nature version 2.1 (MEGAN2.1): An extended and updated framework for modeling biogenic emissions. Geoscientific Model Development 5, 1471-1492, doi:10.5194/gmd-5-1471-2012.

Hansen, J., Sato, M., Ruedy, R., 1997. Radiative forcing and climate response. Journal of Geophysical Research Atmospheres 102, 6831-6864, doi:10.1029/96JD03436.

Heald, C.L., Ridley, D.A., Kroll, J.H., Barrett, S.R.H., Cady-Pereira, K.E., Alvarado, M.J., Holmes,

612 C.D., 2014. Contrasting the direct radiative effect and direct radiative forcing of aerosols.
613 Atmospheric Chemistry and Physics 14, 5513-5527, doi:10.5194/acp-14-5513-2014.

614 Hess, M., Koepke, P., Schult, I., 1998. Optical Properties of Aerosols and Clouds: The Software
615 Package OPAC. Bulletin of the American Meteorological Society 79, 831-844, doi:10.1175/1520-
616 0477(1998)079<0831:OPOAAC>2.0.CO;2.

617 Holben, B.N., Eck, T.F., Slutsker, I., Tanré, D., Buis, J.P., Setzer, A., Vermote, E., Reagan, J.A.,
618 Kaufman, Y.J., Nakajima, T., Lavenu, F., Jankowiak, I., Smirnov, A., 1998. AERONET - A
619 federated instrument network and data archive for aerosol characterization. Remote Sensing of
620 Environment 66, 1-16, doi:10.1016/S0034-4257(98)00031-5.

621 Hudman, R.C., Moore, N.E., Mebust, A.K., Martin, R.V., Russell, A.R., Valin, L.C., Cohen, R.C.,
622 2012. Steps towards a mechanistic model of global soil nitric oxide emissions: Implementation
623 and space based-constraints. Atmospheric Chemistry and Physics 12, 7779-7795,
624 doi:10.5194/acp-12-7779-2012.

625 Jacobson, M.Z., 2001. Strong radiative heating due to the mixing state of black carbon in
626 atmospheric aerosols. Nature 409, 695-697, doi:10.1038/35055518.

627 Jaeglé, L., Quinn, P.K., Bates, T.S., Alexander, B., Lin, J.T., 2011. Global distribution of sea salt
628 aerosols: New constraints from in situ and remote sensing observations. Atmospheric Chemistry
629 and Physics 11, 3137-3157, doi:10.5194/acp-11-3137-2011.

630 Janssens-Maenhout, G., Crippa, M., Guizzardi, D., Dentener, F., Muntean, M., Pouliot, G.,
631 Keating, T., Zhang, Q., Kurokawa, J., Wankmüller, R., Denier Van Der Gon, H., Kuenen, J.J.P.,
632 Klimont, Z., Frost, G., Darras, S., Koffi, B., Li, M., 2015. HTAP-v2.2: A mosaic of regional and
633 global emission grid maps for 2008 and 2010 to study hemispheric transport of air pollution.
634 Atmospheric Chemistry and Physics 15, 11411-11432, doi:10.5194/acp-15-11411-2015.

635 Jimenez, J.L., Canagaratna, M.R., Donahue, N.M., Prevot, A.S.H., Zhang, Q., Kroll, J.H., DeCarlo,
636 P.F., Allan, J.D., Coe, H., Ng, N.L., Aiken, A.C., Docherty, K.S., Ulbrich, I.M., Grieshop, A.P.,
637 Robinson, A.L., Duplissy, J., Smith, J.D., Wilson, K.R., Lanz, V.A., Hueglin, C., Sun, Y.L., Tian, J.,
638 Laaksonen, A., Raatikainen, T., Rautiainen, J., Vaattovaara, P., Ehn, M., Kulmala, M., Tomlinson,
639 J.M., Collins, D.R., Cubison, M.J., Dunlea, E.J., Huffman, J.A., Onasch, T.B., Alfarra, M.R.,
640 Williams, P.I., Bower, K., Kondo, Y., Schneider, J., Drewnick, F., Borrmann, S., Weimer, S.,
641 Demerjian, K., Salcedo, D., Cottrell, L., Griffin, R., Takami, A., Miyoshi, T., Hatakeyama, S.,

642 Shimono, A., Sun, J.Y., Zhang, Y.M., Dzepina, K., Kimmel, J.R., Sueper, D., Jayne, J.T., Herndon,
643 S.C., Trimborn, A.M., Williams, L.R., Wood, E.C., Middlebrook, A.M., Kolb, C.E., Baltensperger,
644 U., Worsnop, D.R., 2009. Evolution of organic aerosols in the atmosphere. Science 326, 1525-
645 1529, doi:10.1126/science.1180353.

646 Jo, D.S., Park, R.J., Kim, M.J., Spracklen, D.V., 2013. Effects of chemical aging on global
647 secondary organic aerosol using the volatility basis set approach. Atmospheric Environment 81,
648 230-244, doi:10.1016/j.atmosenv.2013.08.055.

649 Jo, D.S., Park, R.J., Lee, S., Kim, S.W., Zhang, X., 2016. A global simulation of brown carbon:
650 Implications for photochemistry and direct radiative effect. Atmospheric Chemistry and Physics
651 16, 3413-3432, doi:10.5194/acp-16-3413-2016.

652 Koch, D., Schulz, M., Kinne, S., McNaughton, C., Spackman, J.R., Balkanski, Y., Bauer, S.,
653 Berntsen, T., Bond, T.C., Boucher, O., Chin, M., Clarke, A., De Luca, N., Dentener, F., Diehl, T.,
654 Dubovik, O., Easter, R., Fahey, D.W., Feichter, J., Fillmore, D., Freitag, S., Ghan, S., Ginoux, P.,
655 Gong, S., Horowitz, L., Iversen, T., Kirkevåg, A., Klimont, Z., Kondo, Y., Krol, M., Liu, X.,
656 Miller, R., Montanaro, V., Moteki, N., Myhre, G., Penner, J.E., Perlwitz, J., Pitari, G., Reddy, S.,
657 Sahu, L., Sakamoto, H., Schuster, G., Schwarz, J.P., Seland, Ø., Stier, P., Takegawa, N., Takemura,
658 T., Textor, C., Van Aardenne, J.A., Zhao, Y., 2009. Evaluation of black carbon estimations in
659 global aerosol models. Atmospheric Chemistry and Physics 9, 9001-9026, doi:10.5194/acp-9-
660 9001-2009.

661 Kok, J.F., Ridley, D.A., Zhou, Q., Miller, R.L., Zhao, C., Heald, C.L., Ward, D.S., Albani, S.,
662 Haustein, K., 2017. Smaller desert dust cooling effect estimated from analysis of dust size and
663 abundance. Nature Geoscience 10, 274-278, doi:10.1038/ngeo2912.

664 Lin, G., Penner, J.E., Flanner, M.G., Sillman, S., Xu, L., Zhou, C., 2014. Radiative forcing of
665 organic aerosol in the atmosphere and on snow: Effects of SOA and brown carbon. Journal of
666 Geophysical Research 119, 7453-7476, doi:10.1002/2013JD021186.

667 Liu, D., Whitehead, J., Alfarra, M.R., Reyes-Villegas, E., Spracklen, D.V., Reddington, C.L., Kong,
668 S., Williams, P.I., Ting, Y.C., Haslett, S., Taylor, J.W., Flynn, M.J., Morgan, W.T., McFiggans, G.,
669 Coe, H., Allan, J.D., 2017. Black-carbon absorption enhancement in the atmosphere determined
670 by particle mixing state. Nature Geoscience 10, 184-188, doi:10.1038/ngeo2901.

671 Liu, S., Aiken, A.C., Gorkowski, K., Dubey, M.K., Cappa, C.D., Williams, L.R., Herndon, S.C.,

672 Massoli, P., Fortner, E.C., Chhabra, P.S., Brooks, W.A., Onasch, T.B., Jayne, J.T., Worsnop, D.R.,
673 China, S., Sharma, N., Mazzoleni, C., Xu, L., Ng, N.L., Liu, D., Allan, J.D., Lee, J.D., Fleming,
674 Z.L., Mohr, C., Zotter, P., Szidat, S., Prévôt, A.S.H., 2015. Enhanced light absorption by mixed
675 source black and brown carbon particles in UK winter. Nature Communications 6,
676 doi:10.1038/ncomms9435.

677 Malm, W.C., Sisler, J.F., Huffman, D., Eldred, R.A., Cahill, T.A., 1994. Spatial and seasonal trends
678 in particle concentration and optical extinction in the United States. Journal of Geophysical
679 Research 99, 1347-1370, doi:10.1029/93JD02916.

680 Mishchenko, M.I., Dlugach, J.M., Yanovitskij, E.G., Zakharova, N.T., 1999. Bidirectional
681 reflectance of flat, optically thick particulate layers: An efficient radiative transfer solution and
682 applications to snow and soil surfaces. Journal of Quantitative Spectroscopy and Radiative
683 Transfer 63, 409-432, doi:10.1016/S0022-4073(99)00028-X.

684 Murray, L.T., Jacob, D.J., Logan, J.A., Hudman, R.C., Koshak, W.J., 2012. Optimized regional and
685 interannual variability of lightning in a global chemical transport model constrained by
686 LIS/OTD satellite data. Journal of Geophysical Research Atmospheres 117,
687 doi:10.1029/2012JD017934.

688 Myhre, G., Berglen, T.F., Johnsrud, M., Hoyle, C.R., Berntsen, T.K., Christopher, S.A., Fahey,
689 D.W., Isaksen, I.S.A., Jones, T.A., Kahn, R.A., Loeb, N., Quinn, P., Remer, L., Schwarz, J.P., Yttri,
690 K.E., 2009. Modelled radiative forcing of the direct aerosol effect with multi-observation
691 evaluation. Atmospheric Chemistry and Physics 9, 1365-1392, doi:10.5194/acp-9-1365-2009.

692 Park, R.J., Jacob, D.J., Chin, M., Martin, R.V., 2003. Sources of carbonaceous aerosols over the
693 United States and implications for natural visibility. Journal of Geophysical Research
694 Atmospheres 108, AAC 5-1 - AAC 5-14.

695 Park, R.J., Jacob, D.J., Field, B.D., Yantosca, R.M., Chin, M., 2004. Natural and transboundary
696 pollution influences on sulfate-nitrate-ammonium aerosols in the United States: Implications for
697 policy. Journal of Geophysical Research D: Atmospheres 109, D15204 15201-15217,
698 doi:10.1029/2003JD00473.

699 Park, R.J., Kim, M.J., Jeong, J.I., Youn, D., Kim, S., 2010. A contribution of brown carbon
700 aerosol to the aerosol light absorption and its radiative forcing in East Asia. Atmospheric
701 Environment 44, 1414-1421, doi:10.1016/j.atmosenv.2010.01.042.

Pye, H.O.T., Chan, A.W.H., Barkley, M.P., Seinfeld, J.H., 2010. Global modeling of organic aerosol: The importance of reactive nitrogen (NOx and NO3). Atmospheric Chemistry and Physics 10, 11261-11276, doi:10.5194/acp-10-11261-2010.

Ridley, D.A., Heald, C.L., Ford, B., 2012. North African dust export and deposition: A satellite and model perspective. Journal of Geophysical Research Atmospheres 117, doi:10.1029/2011JD016794.

Schiferl, L.D., Heald, C.L., Nowak, J.B., Holloway, J.S., Andrewneuman, J., Bahreini, R., Pollack, I.B., Ryerson, T.B., Wiedinmyer, C., Murphy, J.G., 2014. An investigation of ammonia and inorganic particulate matter in california during the calnex campaign. Journal of Geophysical Research 119, 1883-1902, doi:10.1002/2013JD020765.

Schultz, D.M., Mikkonen, S., Laaksonen, A., Richman, M.B., 2007. Weekly precipitation cycles? Lack of evidence from United States surface stations. Geophysical Research Letters 34, doi:10.1029/2007GL031889.

Sinyuk, A., Torres, O., Dubovik, O., 2003. Combined use of satellite and surface observations to infer the imaginary part of refractive index of Saharan dust. Geophysical Research Letters 30, 53-51 - 53-54, doi:10.1029/2002GL016189.

Snider, G., Weagle, C.L., Martin, R.V., Van Donkelaar, A., Conrad, K., Cunningham, D., Gordon, C., Zwicker, M., Akoshile, C., Artaxo, P., Anh, N.X., Brook, J., Dong, J., Garland, R.M., Greenwald, R., Griffith, D., He, K., Holben, B.N., Kahn, R., Koren, I., Lagrosas, N., Lestari, P., Ma, Z., Vanderlei Martins, J., Quel, E.J., Rudich, Y., Salam, A., Tripathi, S.N., Yu, C., Zhang, Q., Zhang, Y., Brauer, M., Cohen, A., Gibson, M.D., Liu, Y., 2015. SPARTAN: A global network to evaluate and enhance satellite-based estimates of ground-level particulate matter for global health applications. Atmospheric Measurement Techniques 8, 505-521, doi:10.5194/amt-8-505-2015.

Snider, G., Weagle, C.L., Murdymootoo, K.K., Ring, A., Ritchie, Y., Stone, E., Walsh, A., Akoshile, C., Anh, N.X., Balasubramanian, R., Brook, J., Qonitan, F.D., Dong, J., Griffith, D., He, K., Holben, B.N., Kahn, R., Lagrosas, N., Lestari, P., Ma, Z., Misra, A., Norford, L.K., Quel, E.J., Salam, A., Schichtel, B., Segev, L., Tripathi, S., Wang, C., Yu, C., Zhang, Q., Zhang, Y., Brauer, M., Cohen, A., Gibson, M.D., Liu, Y., Martins, J.V., Rudich, Y., Martin, R.V., 2016. Variation in global chemical composition of PM2.5: emerging results from SPARTAN. Atmospheric Chemistry and

732 Physics 16, 9629-9653, doi:10.5194/acp-16-9629-2016.

733 Spracklen, D.V., Jimenez, J.L., Carslaw, K.S., Worsnop, D.R., Evans, M.J., Mann, G.W., Zhang, Q.,
734 Canagaratna, M.R., Allan, J., Coe, H., McFiggans, G., Rap, A., Forster, P., 2011. Aerosol mass
735 spectrometer constraint on the global secondary organic aerosol budget. Atmospheric Chemistry
736 and Physics 11, 12109-12136, doi:10.5194/acp-11-12109-2011.

737 Stettler, M.E.J., Eastham, S., Barrett, S.R.H., 2011. Air quality and public health impacts of UK
738 airports. Part I: Emissions. Atmospheric Environment 45, 5415-5424,
739 doi:10.1016/j.atmosenv.2011.07.012.

740 Stier, P., Seinfeld, J.H., Kinne, S., Boucher, O., 2007. Aerosol absorption and radiative forcing.
741 Atmospheric Chemistry and Physics 7, 5237-5261, doi:10.5194/acp-7-5237-2007.

742 Toon, O.B., Ackerman, T.P., 1981. Algorithms for the calculation of scattering by stratified
743 spheres. Applied Optics 20, 3657-3660, doi:10.1364/AO.20.003657.

744 Tsigaridis, K., Daskalakis, N., Kanakidou, M., Adams, P.J., Artaxo, P., Bahadur, R., Balkanski, Y.,
745 Bauer, S.E., Bellouin, N., Benedetti, A., Bergman, T., Berntsen, T.K., Beukes, J.P., Bian, H.,
746 Carslaw, K.S., Chin, M., Curci, G., Diehl, T., Easter, R.C., Ghan, S.J., Gong, S.L., Hodzic, A.,
747 Hoyle, C.R., Iversen, T., Jathar, S., Jimenez, J.L., Kaiser, J.W., Kirkeväg, A., Koch, D., Kokkola, H.,
748 H Lee, Y., Lin, G., Liu, X., Luo, G., Ma, X., Mann, G.W., Mihalopoulos, N., Morcrette, J.J., Müller,
749 J.F., Myhre, G., Myriokefalitakis, S., Ng, N.L., O'Donnell, D., Penner, J.E., Pozzoli, L., Pringle,
750 K.J., Russell, L.M., Schulz, M., Sciare, J., Seland, Ø., Shindell, D.T., Sillman, S., Skeie, R.B.,
751 Spracklen, D., Stavrakou, T., Steenrod, S.D., Takemura, T., Tiitta, P., Tilmes, S., Tost, H., Van
752 Noije, T., Van Zyl, P.G., Von Salzen, K., Yu, F., Wang, Z., Wang, Z., Zaveri, R.A., Zhang, H.,
753 Zhang, K., Zhang, Q., Zhang, X., 2014. The AeroCom evaluation and intercomparison of
754 organic aerosol in global models. Atmospheric Chemistry and Physics 14, 10845-10895,
755 doi:10.5194/acp-14-10845-2014.

756 Wang, J.X.L., 2015. Mapping the Global Dust Storm Records: Review of Dust Data Sources in
757 Supporting Modeling/Climate Study. Current Pollution Reports 1, 82-94, doi:10.1007/s40726-
758 015-0008-y.

759 Wang, Y., Zhang, Q.Q., He, K., Zhang, Q., Chai, L., 2013. Sulfate-nitrate-ammonium aerosols
760 over China: Response to 2000-2015 emission changes of sulfur dioxide, nitrogen oxides, and
761 ammonia. Atmospheric Chemistry and Physics 13, 2635-2652, doi:10.5194/acp-13-2635-2013.

762 Yang, M., Howell, S.G., Zhuang, J., Huebert, B.J., 2009. Attribution of aerosol light absorption to
763 black carbon, brown carbon, and dust in China - Interpretations of atmospheric measurements
764 during EAST-AIRE. Atmospheric Chemistry and Physics 9, 2035-2050, doi:10.5194/acp-9-2035-
765 2009.

766 Yu, F., 2011. A secondary organic aerosol formation model considering successive oxidation
767 aging and kinetic condensation of organic compounds: Global scale implications. Atmospheric
768 Chemistry and Physics 11, 1083-1099, doi:10.5194/acp-11-1083-2011.

769 Yu, K., Jacob, D.J., Fisher, J.A., Kim, P.S., Marais, E.A., Miller, C.C., Travis, K.R., Zhu, L.,
770 Yantosca, R.M., Sulprizio, M.P., Cohen, R.C., Dibb, J.E., Fried, A., Mikoviny, T., Ryerson, T.B.,
771 Wennberg, P.O., Wisthaler, A., 2016. Sensitivity to grid resolution in the ability of a chemical
772 transport model to simulate observed oxidant chemistry under high-isoprene conditions.
773 Atmospheric Chemistry and Physics 16, 4369-4378, doi:10.5194/acp-16-4369-2016.

774 Zender, C.S., Bian, H., Newman, D., 2003. Mineral Dust Entrainment and Deposition (DEAD)
775 model: Description and 1990s dust climatology. Journal of Geophysical Research D:
776 Atmospheres 108, AAC 8-1 - AAC 8-19.

777 Zhang, L., Kok, J.F., Henze, D.K., Li, Q., Zhao, C., 2013. Improving simulations of fine dust
778 surface concentrations over the western United States by optimizing the particle size distribution.
779 Geophysical Research Letters 40, 3270-3275, doi:10.1002/grl.50591.

780 Zhang, Q., Jimenez, J.L., Canagaratna, M.R., Allan, J.D., Coe, H., Ulbrich, I., Alfarra, M.R.,
781 Takami, A., Middlebrook, A.M., Sun, Y.L., Dzepina, K., Dunlea, E., Docherty, K., DeCarlo, P.F.,
782 Salcedo, D., Onasch, T., Jayne, J.T., Miyoshi, T., Shimono, A., Hatakeyama, S., Takegawa, N.,
783 Kondo, Y., Schneider, J., Drewnick, F., Borrmann, S., Weimer, S., Demerjian, K., Williams, P.,
784 Bower, K., Bahreini, R., Cottrell, L., Griffin, R.J., Rautiainen, J., Sun, J.Y., Zhang, Y.M., Worsnop,
785 D.R., 2007. Ubiquity and dominance of oxygenated species in organic aerosols in
786 anthropogenically-influenced Northern Hemisphere midlatitudes. Geophysical Research Letters
787 34, doi:10.1029/2007GL029979.

788 Zhu, L., Henze, D., Bash, J., Jeong, G.R., Cady-Pereira, K., Shephard, M., Luo, M., Paulot, F.,
789 Capps, S., 2015. Global evaluation of ammonia bidirectional exchange and livestock diurnal
790 variation schemes. Atmospheric Chemistry and Physics 15, 12823-12843, doi:10.5194/acp-15-
791 12823-2015.

792 Zhu, L., Henze, D.K., Cady-Pereira, K.E., Shephard, M.W., Luo, M., Pinder, R.W., Bash, J.O.,
793 Jeong, G.R., 2013. Constraining U.S. ammonia emissions using TES remote sensing observations
794 and the GEOS-Chem adjoint model. Journal of Geophysical Research Atmospheres 118, 3355-
795 3368, doi:10.1002/jgrd.50166.

796 **Appendix**

797
798
799 Table A1. Descriptions for sensitivity cases used in this study.

Cases	Description			
	BC input parameters from	mixing state assumption	brown carbon	size distribution of soil dust from Zhang et al. (2013)
GEOS_EX	GEOS case	external	X	X
OPAC_EX	OPAC case	external	X	X
BB_EX	BB case	external	X	X
BBR_EX	BBR case	external	X	X
BBHR_EX	BBHR case	external	X	X
GEOS_HI	GEOS case	homogeneous internal	X	X
GEOS_CS	GEOS case	core-shell internal	X	X
OPAC_HI	OPAC case	homogeneous internal	X	X
OPAC_CS	OPAC case	core-shell internal	X	X
GEOS_BR_EX	GEOS case	external	O	X
GEOS_DI_EX	GEOS case	external	X	O
GEOS_BR_DI_EX	GEOS case	external	O	O
BB_BR_DI_EX	BB case	external	O	O
BBR_BR_DI_EX	BBR case	external	O	O
BBHR_BR_DI_EX	BBHR case	external	O	O

800

801 Tables

802
803
804 Table 1. Annual global emissions for anthropogenic and natural sources.

Emission types	Species							Sources
	SO_x [TgS]	NO_x [TgN]	NH_3 [TgN]	BC [TgC]	OC [TgC]	Dust [Tg]	Sea salt [Tg]	
Anthropogenic	55.0	30.0	39.3[1)]	5.5	12.1			HTAPv2
Biomass burning	0.9	4.3	3.3	1.9	16.2			Giglio et al. (2013)
Volcanic	13.9							AeroCom
Oceanic DMS	16.8							Park et al. (2004)
Soil		10.2						Hudman et al. (2012)
Lightning	7.1							Murray et al. (2012)
Aircraft	0.1	0.8						Stettler et al. (2011)
Dust						1165.2		Fairlie et al. (2007)
Sea salt							3321.8	Jaeglé et al. (2011)
Total	86.7	52.5	42.6	7.4	28.3	1165.2	3321.8	

805

Table 2. Physical input values for Mie calculation using FlexAOD. The mean radius (r_g) and standard deviation (σ_g), density (ϱ), the real and imaginary part of refractive indices (RI) at 440 nm and 870 nm, and hygroscopic growth factors (HGFs) for 50% and 95% are presented.

	Inorganics	OC	BC	Sea salt		Dust			
				Accumulation	Coarse	Bin1	Bin2	Bin3	Bin4
r_g (μm)	0.0695[a]	0.073[b]	0.020[c]	0.085[d]	0.401[d]	0.1-1.0	1.0-1.8	1.8-3.0	3.0-6.0
σ_g	1.6[b]	1.6[b]	1.6[b]	1.5[d]	1.8[d]				
ϱ (g cm^{-3})	1.7[e]	1.8[a]	1.8[f]	2.2[a]		2.5	2.65	2.65	2.65
RI at 440 nm	1.53 - 0.005i[a]	1.53 - 0.005i[a]	1.75 - 0.456[a]	$1.50 - 2.54 \times 10^{-8}$i[a]		1.570 - 0.0025i[g]			
RI at 870 nm	1.52 - 0.009i[a]	1.52 - 0.009i[a]	1.75 - 0.435[a]	$1.48 - 3.03 \times 10^{-5}$i[a]		1.540 - 0.0009i[g]			
HGFs at 50%	1.34[a]	1.14[h]	1.00[e]	1.81[a]	1.81[a]	1.0			
HGFs at 95%	1.88[a]	1.35[h]	1.50[e]	2.89[a]	2.92[a]	1.0			

a) Hess et al. (1998)
b) Drury et al. (2010)
c) http://wiki.seas.harvard.edu/geos-chem/
d) Jaeglé et al. (2011)
e) Chin et al. (2002)
f) Bond and Bergstrom (2006)
g) Sinyuk et al. (2003)
h) Jimenez et al. (2009)

819 Table 3. Input parameters for sensitivity simulations of BC.

Cases	refractive index	density [g cm^{-3}]	mean radius [μm]	sigma
GEOS	1.74 - 0.44i	1.8	0.02	1.6
OPAC	1.74 - 0.44i	1.0	0.0118	2.0
BB	1.95 - 0.79i	1.8	0.02	1.6
BBR	1.95 - 0.79i	1.8	0.065	1.6
BBHR	1.95 - 0.79i	1.8	0.1	1.6

820
821
822

823 Table 4. Statistical results of the evaluation of aerosol mass concentrations using two
824 global observation networks. The reduced major axis method was used for the regression
825 slopes.

Observation network	Species	R[a]	Slope	Yict[b]	NMB[c]	RMSE[d]
AMS	Sulfate	0.78	0.77	1.31	0.17	2.25
	Nitrate	0.62	0.84	0.68	0.40	2.04
	Ammonium	0.78	0.69	0.71	0.21	1.18
	Organics	0.36	0.59	0.18	-0.37	4.77
SPARTAN	Sulfate	0.48	0.75	1.02	-0.05	3.84
	Nitrate	0.68	3.60	0.45	2.92	7.66
	Ammonium	0.59	1.72	0.48	1.01	3.03
	BC	0.94	-0.80	0.47	-0.37	2.20
	Dust	0.38	1.14	-1.88	-0.25	6.00
	$PM_{2.5}$	0.76	0.70	2.37	-0.24	21.65

826 a) R: correlation coefficient
827 b) Yict: y-axis intercept
828 c) NMB: normalized mean bias
829 d) RMSE: root mean square error

830 Table 5. Statistical values for the sensitivity simulation of SSA at 440 nm. The observed
831 mean SSA was 0.89. AOD > 0.4 data were only used.

Cases	R[a]	Mean	Slope	Yict[b]	RMSE[c]	Mean bias
GEOS_EX	0.50	0.94	0.38	0.60	0.06	0.06
OPAC_EX	0.52	0.93	0.53	0.45	0.05	0.04
BB_EX	0.53	0.93	0.45	0.53	0.05	0.05
BBR_EX	0.49	0.94	0.38	0.61	0.06	0.06
BBHR_EX	0.38	0.95	0.39	0.61	0.07	0.06
GEOS_HI	0.13	0.85	2.18	-1.08	0.07	-0.04
GEOS_CS	0.14	0.84	2.03	-0.96	0.07	-0.05
OPAC_HI	0.07	0.81	2.98	-1.83	0.11	-0.08
OPAC_CS	0.09	0.82	2.53	-1.43	0.10	-0.07
GEOS_BR_EX	0.56	0.93	0.55	0.44	0.05	0.04
GEOS_DI_EX	0.34	0.94	0.67	0.34	0.06	0.05
GEOS_BR_DI_EX	0.53	0.92	0.70	0.30	0.04	0.03
BB_BR_DI_EX	0.57	0.91	0.75	0.24	0.03	0.02
BBR_BR_DI_EX	0.52	0.92	0.69	0.31	0.04	0.03
BBHR_BR_DI_EX	0.46	0.93	0.68	0.32	0.05	0.04

832 a) R: correlation coefficient
833 b) Yict: y-axis intercept
834 c) RMSE: root mean square error
835
836

837 Table 6 Same as Table 5 except the SSA is at 870 nm. The observed mean SSA was 0.92.

Cases	R[a]	Mean	Slope	Yict[b]	RMSE[c]	Mean bias
GEOS_EX	0.76	0.92	1.17	-0.16	0.03	0.01
OPAC_EX	0.77	0.90	1.63	-0.60	0.04	-0.02
BB_EX	0.77	0.91	1.45	-0.42	0.03	-0.01
BBR_EX	0.77	0.90	1.49	-0.46	0.04	-0.01
BBHR_EX	0.77	0.91	1.35	-0.33	0.03	-0.01
GEOS_HI	0.70	0.90	1.58	-0.56	0.04	-0.02
GEOS_CS	0.73	0.87	1.83	-0.81	0.06	-0.05
OPAC_HI	0.72	0.87	2.09	-1.05	0.07	-0.05
OPAC_CS	0.74	0.84	2.28	-1.25	0.09	-0.08
GEOS_BR_EX	0.76	0.92	1.16	-0.14	0.03	0.01
GEOS_DI_EX	0.79	0.91	1.15	-0.14	0.02	-0.01
GEOS_BR_DI_EX	0.79	0.91	1.10	-0.10	0.02	-0.01
BB_BR_DI_EX	0.79	0.89	1.37	-0.37	0.04	-0.03
BBR_BR_DI_EX	0.80	0.89	1.41	-0.40	0.04	-0.03
BBHR_BR_DI_EX	0.80	0.90	1.27	-0.27	0.03	-0.02

838 a) R: correlation coefficient
839 b) Yict: y-axis intercept
840 c) RMSE: root mean square error
841
842

843 **Figures**

844
845

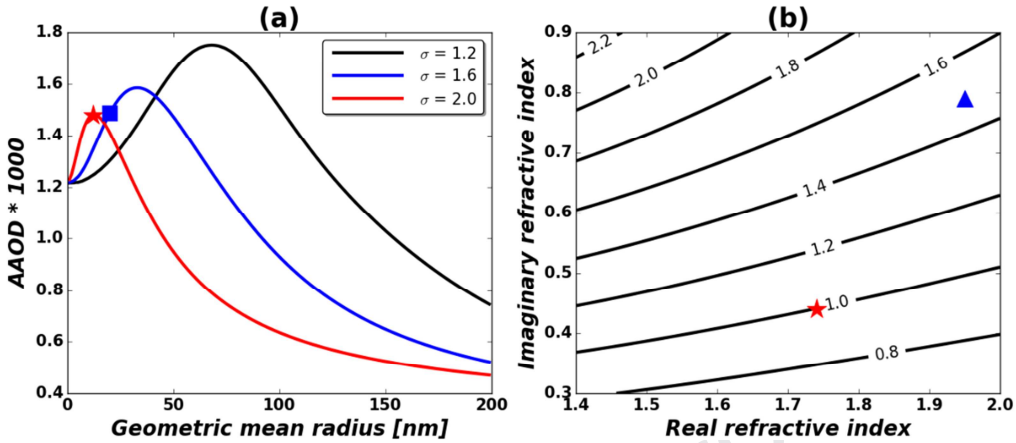

846
847 Fig. 1. (a) Sensitivity results of the mean radius (x-axis) and standard deviations (lines) for
848 BC to AAOD (y-axis) at 550 nm. The blue rectangle and red star indicate GEOS-Chem
849 baseline and OPAC, respectively. The 1.95 – 0.79i were used for the real and imaginary
850 parts of refractive indices, respectively. (b) Sensitivity results of black carbon AAOD
851 (contour line, multiplied by 1000) as a function of the real (x-axis) and imaginary (y-axis)
852 parts of refractive indices. The blue rectangle and red star represent BC AAODs using
853 refractive indices by Bond and Bergstrom (2006) and OPAC, respectively. For both plots,
854 the hygroscopic growth factor of BC was not considered. The density of 1.8 g cm^{-3} and a
855 column concentration of 0.25 mg m^{-2} were used.

856

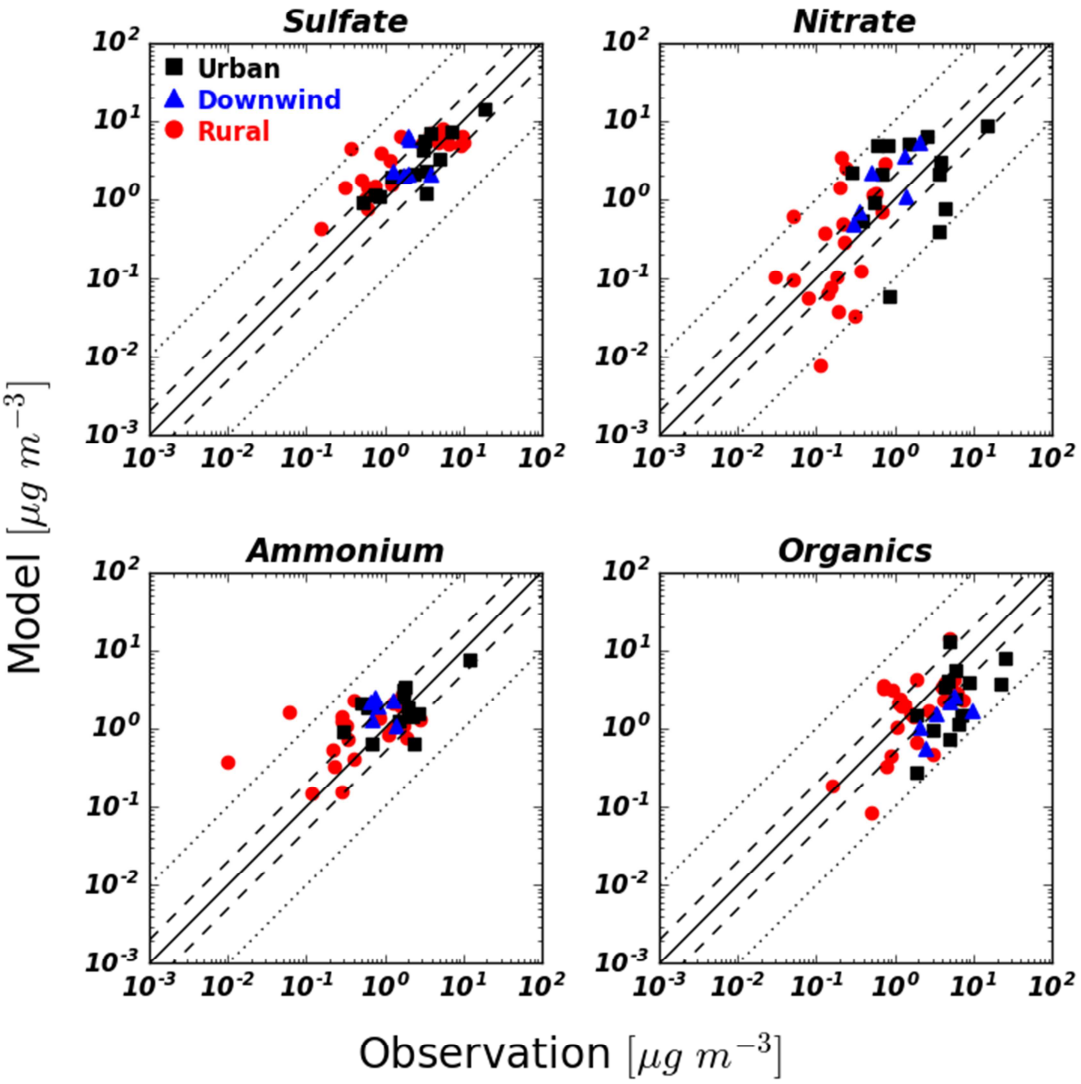

857
858 Fig. 2. Scatterplots of the observed and simulated aerosol concentrations at AMS sites.
859 The 1:1 line, 1:2 lines, and 1:10 lines are inset.

860

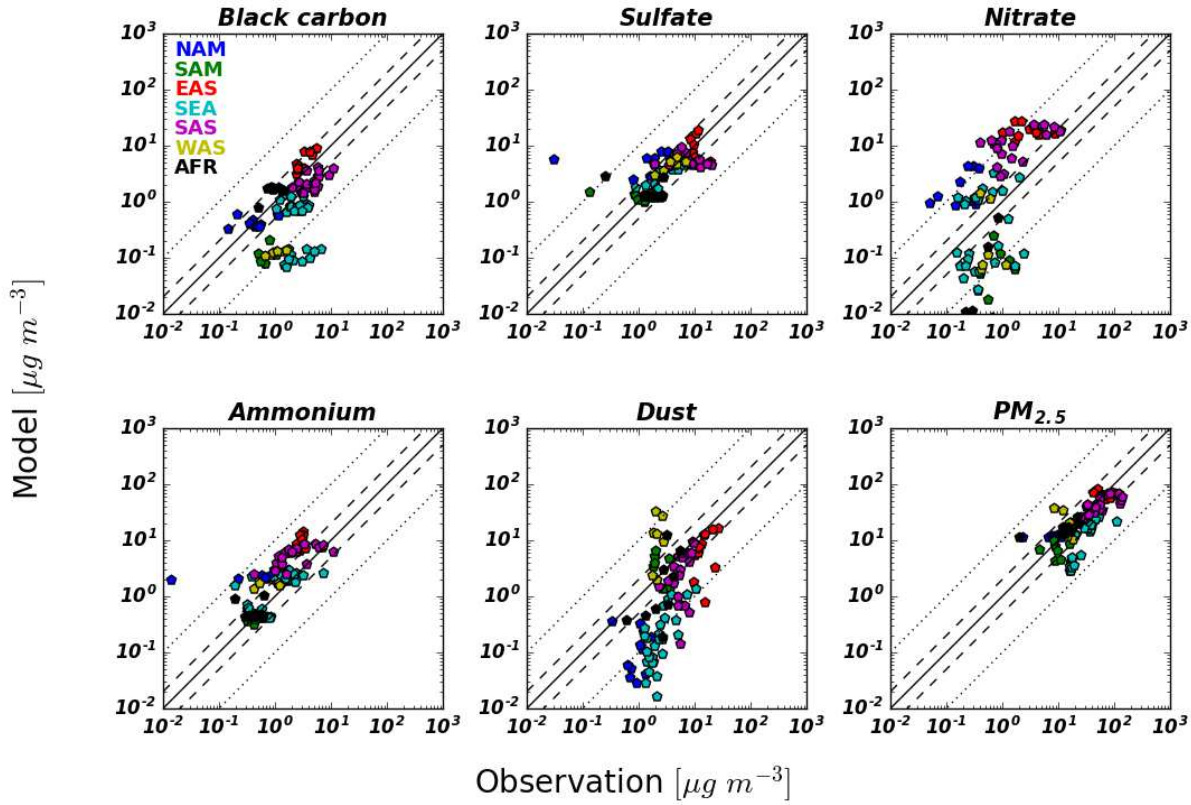

Fig. 3. Scatterplots of the observed and simulated aerosol concentrations at SPARTAN sites. Colors indicate different regions: North America (NAM; blue), South America (SAM; green), East Asia (EAS; red), Southeast Asia (SEA; cyan), South Asia (SAS; magenta), West Asia (WAS, yellow), and Africa (AFR; black). The 1:1 line, 1:2 lines, and 1:10 lines are inset.

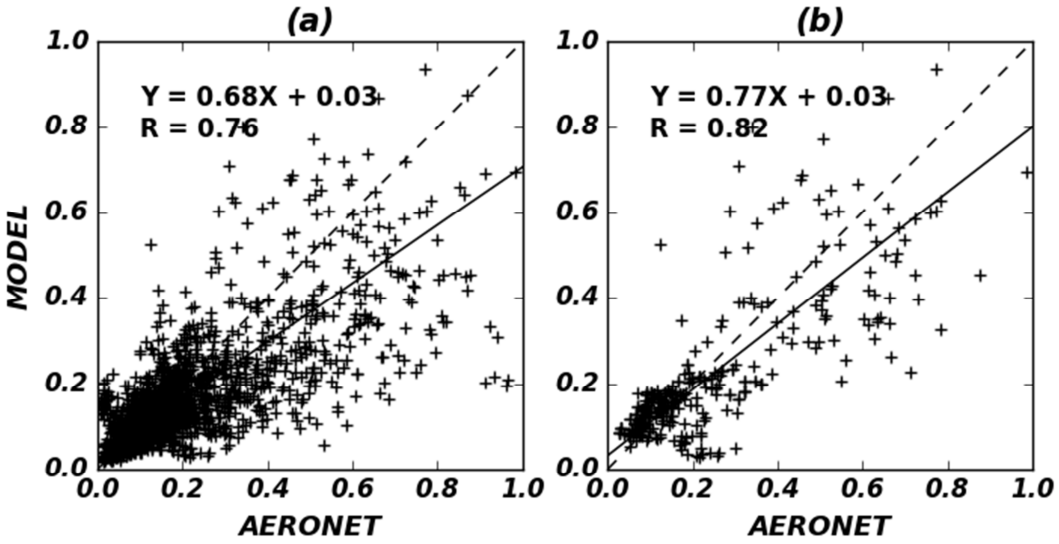

870
871 Fig. 4. Scatterplots of the observed and simulated monthly mean AOD at 500 nm for (a)
872 all AERONET data and (b) selected AERONET data by two criteria for the AMS and
873 SPARTAN data.
874

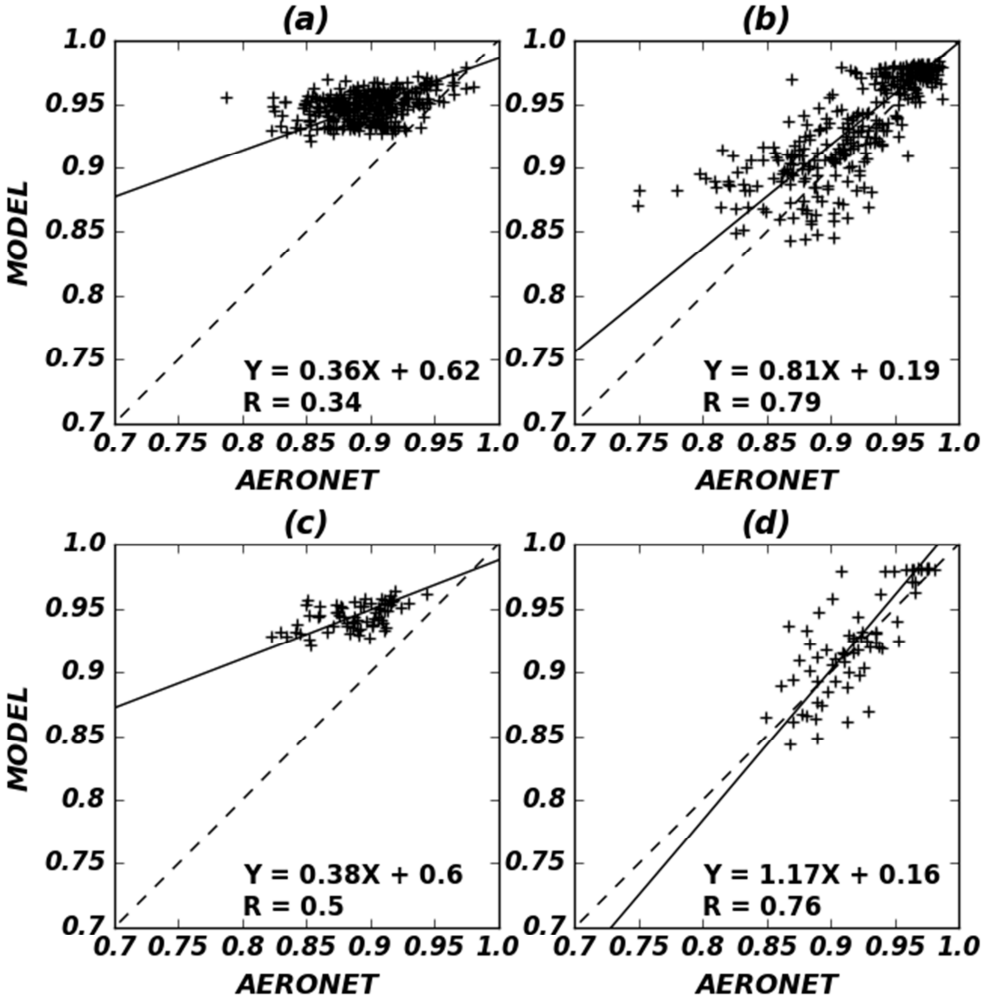

875
876 Fig. 5. Scatterplots of the observed and simulated monthly mean SSA at 440 nm (a, c)
877 and 870 nm (b, d). All AERONET data were used for a) and b), and selected AERONET
878 data were used for c), and d).
879

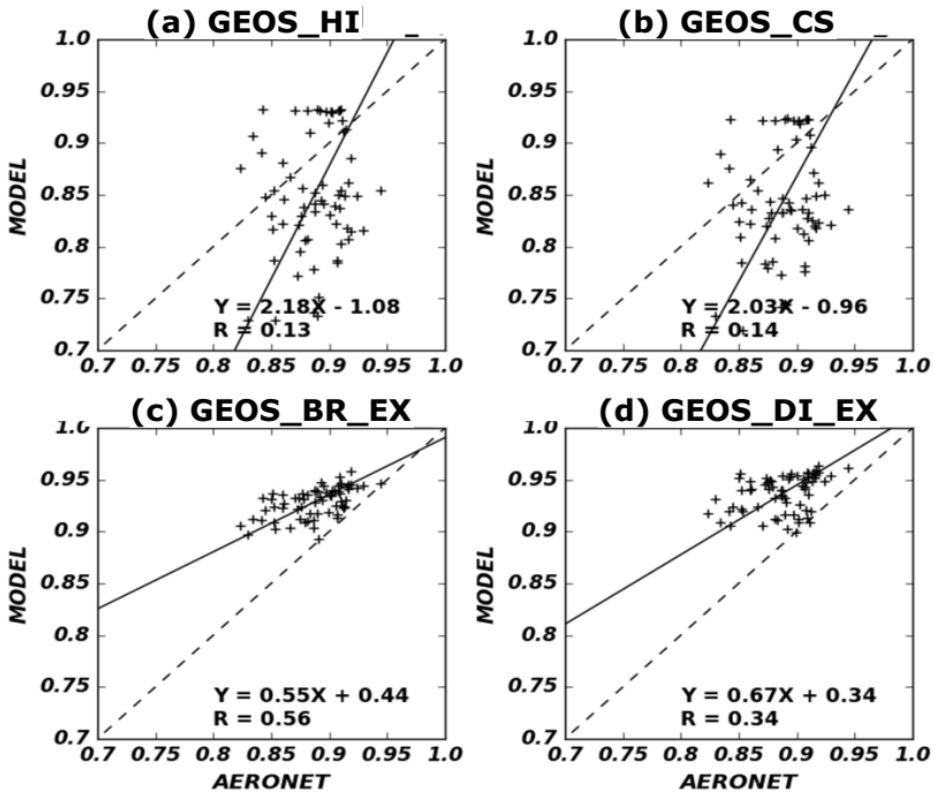

880
881 Fig. 6. Scatterplots of the observed versus simulated monthly mean SSA at 440 nm for
882 sensitivity experiments of (a) homogeneous internal mixing assumption (GEOS_HI), (b)
883 core-shell internal mixing assumption (GEOS_CS), (c) brown carbon absorption with
884 external mixing assumption (GEOS_BR_EX), and (d) observationally-constrained dust
885 size distribution with external mixing assumption (GEOS_DI_EX).
886

887

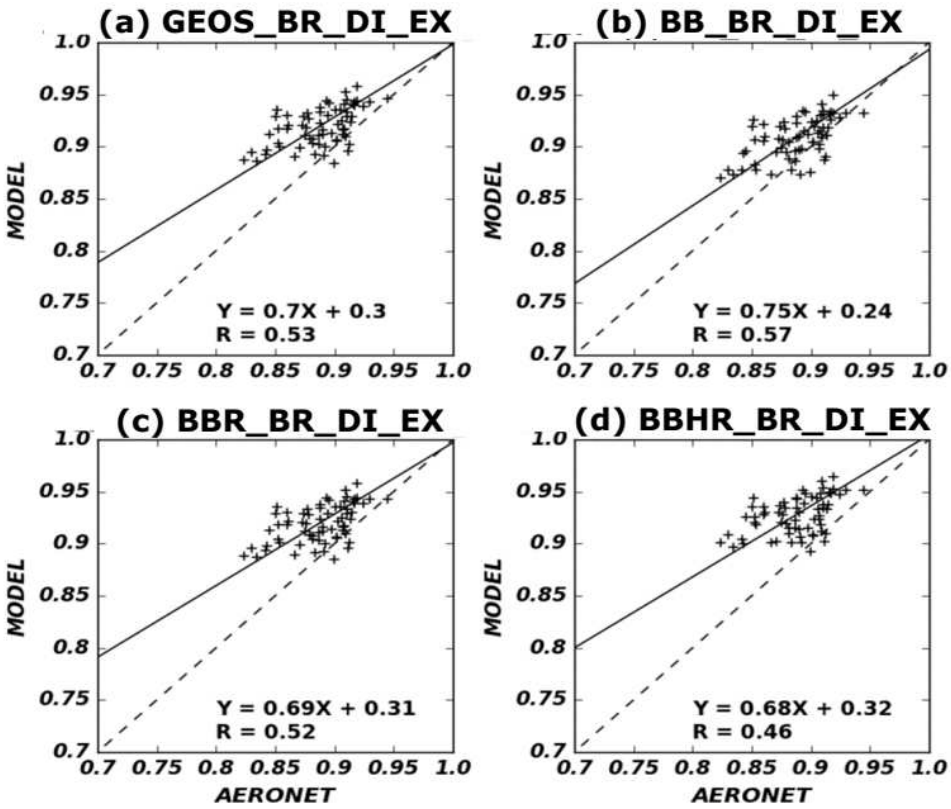

888

889 Fig. 7. Scatterplots of the observed versus simulated monthly mean SSA at 440 nm for
890 sensitivity simulations of BC input parameters from (a) GEOS, (b) BB, (c) BBR, and (d)
891 BBHR. BR_DI_EX denotes the brown carbon, dust size distribution, and external
892 mixing assumption.

893

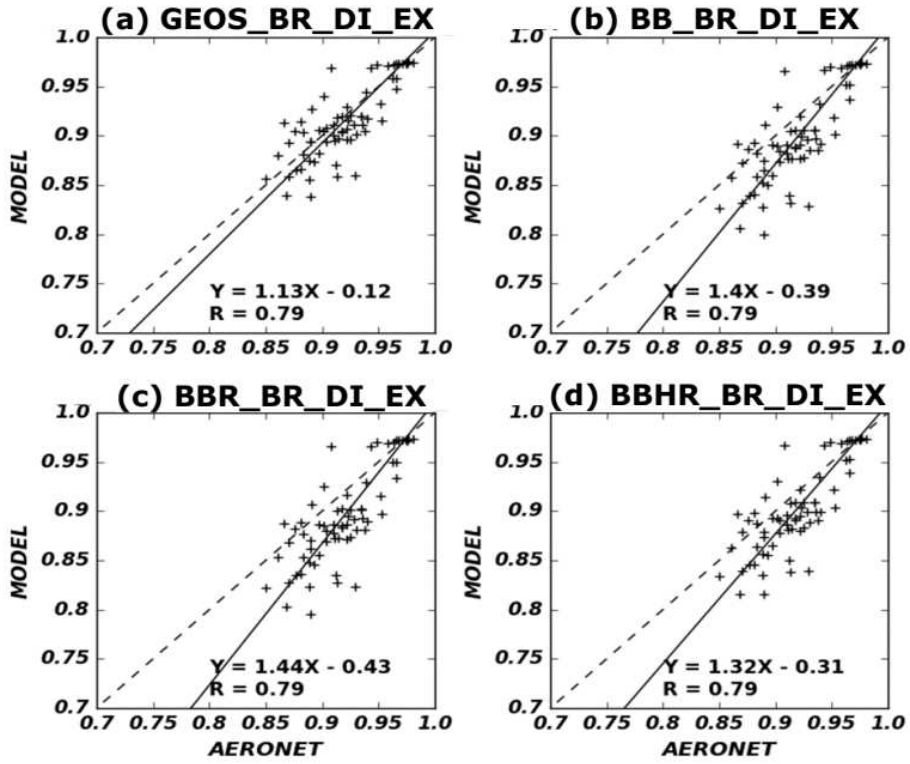

894
895 Fig. 8. Same as Fig. 7, except for SSA at 870 nm.

896

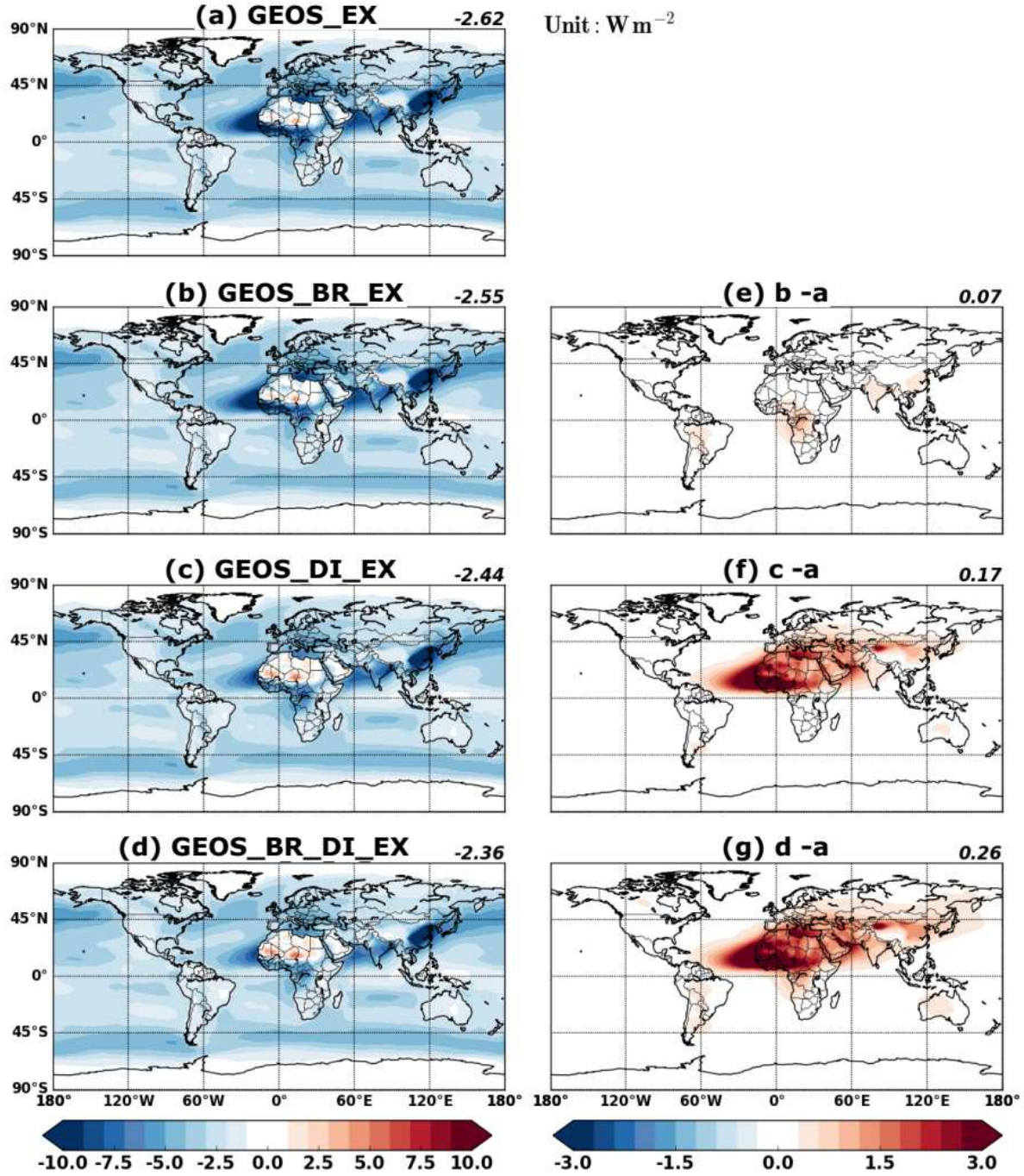

Fig. 9. Sensitivity results of annual mean DRE of the (a) GEOS_EX, (b) GEOS_BR_EX, (c) GEOS_DI_EX, and (d) GEOS_BR_DI_EX cases at the top of the atmosphere. Differences between the GEOS_EX case and each sensitivity are shown in the right panel (e, f, and g).

Highlights

- Single scattering albedo (SSA) has different characteristics at 440 and 870 nm.
- Black carbon density is an important factor in SSA estimation.
- Brown carbon absorption and dust size distribution reduce SSA at 440 nm.
- Mixing state and refractive index of aerosols affect SSA values.
- Correcting SSA bias increases aerosol direct radiative effect (DRE) by 10%.

Declaration of interests

☒ The authors declare that they have no known competing financial interests or personal relationships that could have appeared to influence the work reported in this paper.

☐The authors declare the following financial interests/personal relationships which may be considered as potential competing interests: